Progress In Electromagnetics Research B, Vol. 72, 1–16, 2017

Channel Measurement Based Antenna Synthesis for Mobile Automotive MIMO Communication Systems

Tobias Mahler*, Jerzy Kowalewski, Benjamin Nuß, Cornelius Richt, Jonathan Mayer, and Thomas Zwick

Abstract—In this paper a multiple input multiple output (MIMO) radio channel measurement system is presented that utilizes several software defined radio (SDR) platforms at the transmitter and at the receiver. The system hardware buildup and its calibration technique are presented. The channel measurement results are afterwards exploited for a special antenna synthesis method that was already proofed by raytracing channel simulations. The antenna synthesis method is applied to a mobile single and to a mobile multiple channel receiver. The resulting synthesized antenna systems are evaluated in terms of antenna radiation patterns and the corresponding channel capacities. The results reveal the superiority of synthesized antenna systems compared to conventional omnidirectional antenna systems in the considered urban street scenario. Moreover, the findings from the antenna synthesis based on dynamically measured MIMO radio channels confirm the results from the raytracing channel simulation based antenna synthesis.

1. INTRODUCTION

Multiple antenna systems in wireless communications can bring large increases in the spectral efficiency [1]. Channel knowledge is the key to a systematic improvement of the design of mobile multiple antenna systems. It can not only help to adaptively improve the matching between multiple antenna systems, like phased arrays, and the current multiple input multiple output (MIMO) channel. It is also fundamental to know basic channel properties as for instance predominant directions of reception during the hardware design of non-adaptive antenna elements. This knowledge can either be achieved by channel simulations or by channel measurements, and it can help to achieve design guidelines for mobile multiple antenna systems.

A lot of work has been done in multipath channel sounding and channel characterization [2–5] with high-accuracy measurements [6, 7]. They achieve amazing delay resolutions and spatial resolutions by conducting broadband measurements with highly directional antennas. This work is of great importance when analyzing single multipath components that together constitute the mobile radio channel. But it is problematic to derive individual design guidelines for commercial mobile MIMO antennas on basis of these measurements.

In this paper, a channel sampling is presented to obtain measurement based antenna design guidelines with the help of a special antenna synthesis approach. The key point of this antenna synthesis is that it already comprises the constraints of the desired antenna system to be designed, e.g., the number of antennas, their geometrical sizes, polarization, mounting positions and frequency. Hereby we determine non-adaptive (fixed) antenna radiation patterns that optimize the channel capacity and that are still realizable within a limited available volume at a specific frequency. We achieve this purpose without high-precision measurements of multipath delays and of angles of arrival or departure.

Received 15 August 2016, Accepted 12 November 2016, Scheduled 29 November 2016

* Corresponding author: Tobias Mahler (tobias.mahler@kit.edu).

The authors are with the Institute of Radio Frequency Engineering and Electronics (IHE), Karlsruhe Institute of Technology (KIT), Karlsruhe 76131, Germany.

In addition, it may even be possible to reduce the hardware cost of a system by employing synthesized antenna systems that need fewer hardware paths at the transmitter or receiver to provide the same throughput performance of e.g., an adaptively controlled phased array. The antenna synthesis approach has been published in [8] and has already been applied to simulated channels [9, 10]. In this work, we advance in applying the antenna synthesis on dynamically measured channels for the first time.

To gather the channel information, we first present a channel measurement system based on software defined radio (SDR) platforms. SDRs are small devices, with low power consumption and reasonable initial cost that enable mobile channel measurements. SDRs cannot catch up with the high dynamic range and phase and amplitude stability of network analyzers respectively spectrum analyzers and of the channel sounders employed in [2–4]. But in this work we develop a MIMO channel measurement system based on SDRs, which includes the calibration and reaches the performance necessary for the application of the antenna synthesis approach.

The remainder of this paper is organized as follows. Section 2 describes the channel measurement approach, and Section 3 depicts the measurement system model together with the system calibration. Our channel measurement system buildup is described in Section 4 together with basic measurement results in Section 5. We continue with the antenna synthesis procedure in Section 6 and the antenna synthesis results in Section 7 and finally conclude our work in Section 8.

2. CHANNEL MEASUREMENT APPROACH

The basic principle of measuring a channel is to transmit data, respectively signals, that are already known to the receiver. The receiver is then able to determine the influence, that the channel had on the received signals by simply dividing the received signal by the transmitted one. In fact, no communication takes place because no new information is sent or received. But this technique is widely used even in pilot signals of communication systems in order to gain channel information for the equalization of received signals.

2.1. Hardware Setup

The hardware of the system consists of $M = 4$ parallel transmit paths and $N = 4$ parallel receive paths processing the pilot signals that are used for channel measurements. Its maximum operating frequency is 6 GHz, and it is designed for the purpose of mobile MIMO channel measurements in a fixed-to-mobile setup as for example a base station communicating with a vehicle (see Fig. 1) or in a mobile-to-mobile setup as for example in vehicle-to-vehicle (V2V) communication. Each path is realized by the use of a SDR platform (see Fig. 2). There is also an additional Rx path at the transmit site and an additional Tx path at the receive site of the link. They realize the reference signals needed to calibrate the transmitter hardware through predistortion and to calibrate the receiver hardware through equalization (see Section 3). The calibration stages comprise passive distribution networks to extract the Tx reference signals from the pilots to be transmitted and to add the Rx reference signal to the received pilots. For this purpose the calibration stages comprise power dividers, power combiners and cables that have equal complex transmission factors in order not to impose any imbalances between paths. All transmitting paths throughout the system are called frontends, and all receiving paths are called backends since the system is mainly built for channel measurements and not for data transmission.

The overall goal of this system is to determine the MIMO channel matrix $\mathbf{H}$ as precisely as possible by the use of pilot signals. For this purpose, $\mathbf{H}$ is defined as the matrix of complex transmission factors between the feeding point of each transmit antenna and the feeding point of each receive antenna (see Fig. 2). During operation the complex baseband pilot signals are continuously streamed from the Tx host PC to the Tx SDR platforms and from the Rx SDR platforms to the Rx host PC. The reference signals are in each case streamed in an opposite direction to the pilot signals: The Tx reference signals get extracted from the transmit pilots at the Tx calibration stage and are then fed back into the Tx reference backend for predistortion of the pilots. The Rx reference signal is generated in the Rx reference frontend and added to the received pilot signals at the Rx calibration stage and is then received for equalization of the pilots. Both predistortion and equalization algorithms are implemented in the corresponding host PC software.

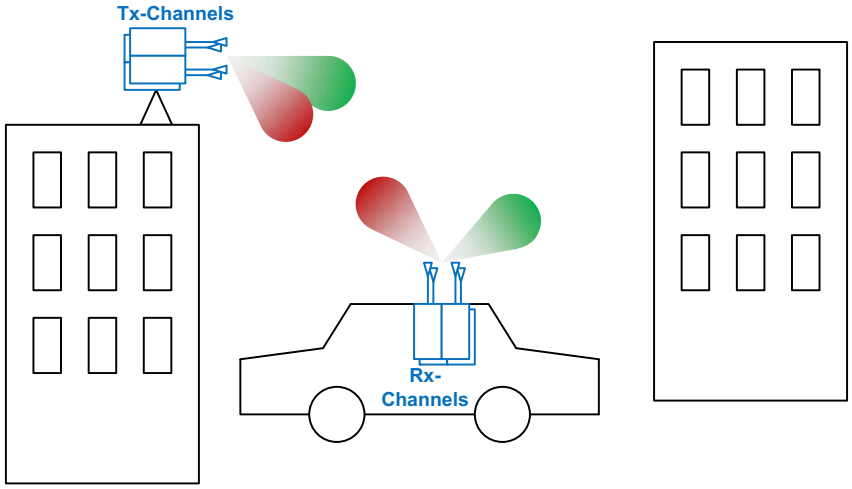

Figure 1. 4×4 MIMO channel measurement system setup.

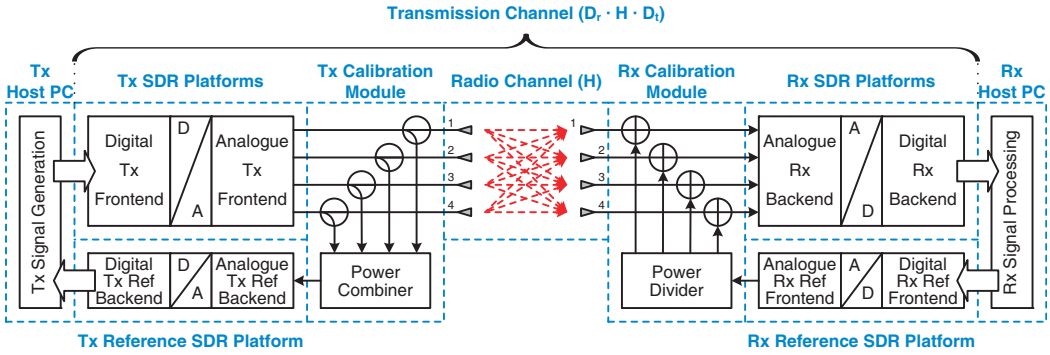

Figure 2. Channel measurement system block diagram.

2.2. Modulation, Waveform and Multiple Access Method

The pilot and reference signals are modulated using the orthogonal frequency-division multiplexing (OFDM) method. To separate the different transmitters and the Rx reference signal, we use different orthogonal OFDM subcarriers, which is called orthogonal frequency-division multiple access (OFDMA). This approach is similar to the transmitter multiplexing that was employed in [11] and [12]. One exemplary receive signal in baseband frequency domain is displayed in Fig. 3. Each transmitter and the Rx reference have their own exclusive OFDM subcarriers, that ideally do not cause any crosstalk between each other. The allocation of the subcarriers is achieved by a simple interleaving scheme, that is displayed in Fig. 3. The Tx reference does not need any dedicated OFDM subcarriers since it only consists of the extracted Tx pilot signals. With this simple OFDMA principle it is always possible to separate the pilot signals that belong to different transmitters. Like this the complete MIMO channel matrix $\mathbf{H}$ can be determined at the Rx host PC.

But the subcarrier frequency separation per transmitter has to stay within some bounds. The minimum coherence bandwidth of the mobile channels to be measured defines the upper limit of the maximum frequency separation in order not to cause any undersampling in frequency domain during channel measurements.

According to that we also have to take the minimum coherence time of the mobile channels to be measured into account. In our case we simply repeat one predefined OFDM symbol in time domain again and again without any gap. This symbol is known to the transmitter and to the receiver and it is additionally optimized in terms of peak-to-average power ratio (PAPR). Thus there are advantages

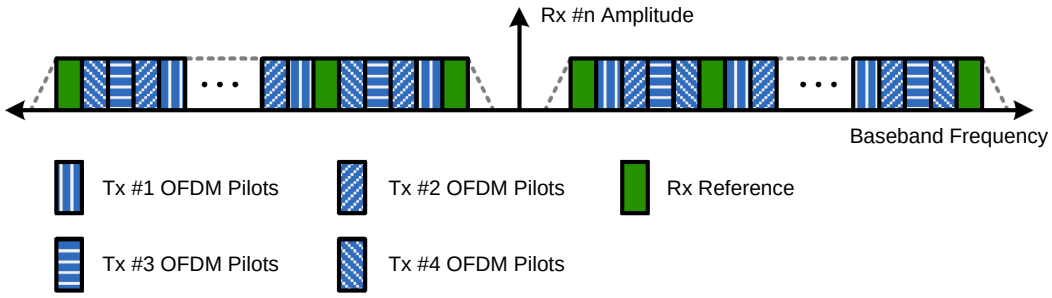

Figure 3. Channel measurement system waveform.

in terms of channel measurement: We do not need any temporal frame synchronization at the receiver site and we can omit the cyclic prefix because the channel is already tuned due to the preceding OFDM symbols. With this signal design the maximum duration of the OFDM symbol is limited by the coherence time of the mobile channels to be measured in order not to cause any undersampling in time domain during channel measurements.

Staying within the coherence time and coherence bandwidth allows a linear interpolation of the amplitude and phase of the frequency bins missing due to OFDMA after completion of the channel measurements. This provides the frequency-dependent and time-dependent MIMO channel matrix $\mathbf{H}(f,t)$.

2.3. Channel Estimation Procedure

The channel estimation is carried out by a least squares estimation algorithm with the narrowband quasistatic MIMO model equation [13]

$$\vec{y} = \mathbf{H} \cdot \vec{x} + \vec{r} \tag{1}$$

and the estimation result

$$\mathbf{H} = \vec{y} \cdot \vec{x}^{\dagger} \cdot \left(\vec{x} \cdot \vec{x}^{\dagger} \right)^{-1} \tag{2}$$

that performs a division of the received signal by the transmitted signal. $\vec{x} \in \mathbb{C}^{M \times 1}$ and $\vec{y} \in \mathbb{C}^{N \times 1}$ are the vectors of transmit and receive signals and $\vec{r} \in \mathbb{C}^{N \times 1}$ is noise. $(\cdot)^{\dagger}$ denotes the complex conjugate transpose. This algorithm can either be used to estimate the channel for each OFDM symbol and each OFDM subcarrier or we can define clusters of several OFDM symbols and/or OFDM subcarriers that deliver one single channel estimation (see Fig. 4). The MIMO channel matrix $\mathbf{H}$ consists of NM elements. Each elements is a matrix itself, namely the OFDM frame submatrix $\mathbf{h}_{nm}$, that contains N_{fr} frequency realizations and N_{tr} time realizations. The easiest way is to apply the estimation on the entire OFDM frame submatrix $\mathbf{h}_{nm}$. But depending on the symbol duration and on the bandwidth used, there might be significant changes over time and/or frequency, that should not be merged into one single channel estimation point. In this case, we define a coherent OFDM submatrix $\mathbf{h}_{nm_{n_{fr}n_{tr}}}$ that contains N_c OFDM subcarriers and N_s OFDM symbols. The constraints to ensure that $\mathbf{h}_{nm_{n_{fr}n_{tr}}}$ contains coherent elements in both dimensions are

$$N_s \cdot T_s \leq T_{\text{coh}} \tag{3}$$

$$N_c \cdot \Delta f \leq B_{\text{coh}}. \tag{4}$$

Reasonable values for the coherence bandwidth B_{coh} and the coherence time T_{coh} of the channel may be looked up in literature or estimated via expected delay spread and doppler spread values of the channel under consideration.

Apply the MIMO OFDM channel estimation on these blocks of N_s OFDM symbols and N_c OFDM subcarriers, then keep coherency in time and frequency dimension, and prevent potential undersampling of the channel characteristics. As a result, the estimation delivers N_{fr} frequency realizations and N_{tr} time realizations of the $N \times M$ MIMO radio channel matrix $\mathbf{H}$.

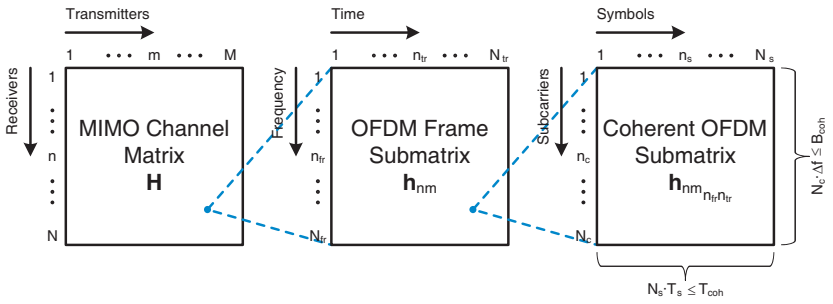

Figure 4. MIMO OFDM matrices for channel estimation.

3. SYSTEM MODEL AND CALIBRATION

The goal is to determine the radio channel matrix $\mathbf{H}$ without any amplitude or phase influences that originate from frontend and backend hardware effects. These effects can be modeled with the help of complex diagonal deviation matrices $\mathbf{D}_t$ at the transmitter and $\mathbf{D}_r$ at the receiver, that describe the amplitude $\mathbf{A}_t$, $\mathbf{A}_r$ and phase $\mathbf{\Phi}_t$, $\mathbf{\Phi}_r$ differences between the paths:

$$\mathbf{D}_t = \mathbf{A}_t \cdot \mathbf{\Phi}_t \tag{5}$$

$$\mathbf{D}_r = \mathbf{A}_r \cdot \mathbf{\Phi}_r \tag{6}$$

The relation between the measured transmission channel matrix $\mathbf{H}_{\text{meas}}$ and the desired radio channel matrix $\mathbf{H}$ can now be determined with the help of these deviation matrices:

$$\mathbf{H}_{\text{meas}} = \mathbf{D}_r \cdot \mathbf{H} \cdot \mathbf{D}_t = \mathbf{A}_r \cdot \mathbf{\Phi}_r \cdot \mathbf{H} \cdot \mathbf{A}_t \cdot \mathbf{\Phi}_t = \begin{pmatrix} d_{r1} & \cdots & 0 \\ \vdots & \ddots & \vdots \\ 0 & \cdots & d_{rN} \end{pmatrix} \cdot \mathbf{H} \cdot \begin{pmatrix} d_{t1} & \cdots & 0 \\ \vdots & \ddots & \vdots \\ 0 & \cdots & d_{tM} \end{pmatrix} \tag{7}$$

The diagonal elements of $\mathbf{D}_t$ and $\mathbf{D}_t$ are in detail

$$d_{tm} = \alpha_{tm} \cdot e^{j \cdot \varphi_{tm}} \tag{8}$$

$$d_{rn} = \alpha_{rn} \cdot e^{j \cdot \varphi_{rn}}. \tag{9}$$

$\mathbf{H}_{\text{meas}}$ and $\mathbf{H}$ are elements of $\mathbb{C}^{N \times M}$. M is the number of transmit antennas and N the number of receive antennas with their index values m and n. α_{tm} and α_{rn} are the deviations between paths in amplitude, and φ_{tm} and φ_{rn} are the corresponding deviations between paths in phase. The intention of the system calibration is to determine

$$\mathbf{H} = \mathbf{D}_r^{-1} \cdot \mathbf{H}_{\text{meas}} \cdot \mathbf{D}_t^{-1} \tag{10}$$

with the aid of the above mentioned predistortion $\mathbf{D}_t^{-1}$ and equalization $\mathbf{D}_r^{-1}$. As a result, we obtain the desired radio channel matrix $\mathbf{H}$ without any hardware influences as they were included in the transmission channel matrix $\mathbf{D}_r \cdot \mathbf{H} \cdot \mathbf{D}_t$ (see Fig. 2).

The described dynamic calibration is applied to each OFDM subcarrier in frequency dimension and to each OFDM symbol in time dimension. Mutual coupling between the paths is not included in this calibration procedure and should already be dodged in hardware.

3.1. Predistortion at the Transmitter

The predistortion at the transmitter site shifts the calibration level from the output of the Tx host PC to the feeding point of the transmit antennas. Since the Tx reference signal contains all subcarriers except the Rx reference subcarriers, there is no frequency interpolation needed. The predistortion therefore is straightforward by multiplying the transmit signal $\vec{x}$ with $\mathbf{D}_t^{-1}$ from the left:

$$\vec{y} = \mathbf{H}_{\text{meas}} \cdot \mathbf{D}_t^{-1} \cdot \vec{x} + \vec{r} \tag{11}$$

3.2. Equalization at the Receiver

The equalization at the receiver site shifts the calibration level from the Rx host PC input to the feeding point of the receive antennas. First the modulation is removed from the pilot carriers and also from the Rx reference carriers. Afterwards, an interpolation over frequency is calculated to obtain the frequency bins that are missing due to the OFDMA principle (see Fig. 3). The equalization then is straightforward by multiplying the pilots of the received signal $\vec{y}$ with $\mathbf{D}_r^{-1}$ from the left:

$$\mathbf{D}_r^{-1} \cdot \vec{y} = \underbrace{\mathbf{D}_r^{-1} \cdot \mathbf{H}_{\text{meas}} \cdot \mathbf{D}_t^{-1}}_{\mathbf{H}} \cdot \vec{x} + \mathbf{D}_r^{-1} \cdot \vec{r} \tag{12}$$

There is a power scaling implemented in the receiver processing to accurately determine the amplitude damping $|\mathbf{H}|$ of the channel: The power of the transmitted pilot signals P_t in the Tx calibration module and the power of the inserted Rx reference signal $P_{r,ref}$ in the Rx calibration module have to be measured before channel measurements and stored for power scaling. The power measurement is carried out once with the aid of a spectrum analyzer or a power meter.

4. SYSTEM BUILDUP AND VERIFICATION

Figure 5 gives an overview of the measurement system buildup, and the basic system parameters are summarized in Table 1. We measure with a 4×4 MIMO system in the ISM frequency band with a center frequency of 2.49175 GHz. The frontend and backend electronics are realized by the use of several SDRs that communicate with the host PC via an ethernet host network [14]. The baseband processing is realized in the host PC software. For mobile frequency and timing reference, several SDRs are cascaded with the same clock reference and GPS disciplined local oscillators that are fed by GPS antenna signals. Additional external amplifiers at the transmitters and at the receivers provide appropriate signal-to-noise ratio (SNR) values during the measurements. The current GPS position of the mobile receiver is continuously logged for subsequent measurement analysis.

The stationary transmitter buildup acts as the base station and was placed on the roof of a building (see Fig. 6(a)). The linear transmit antenna array consists of $M = 4$ patch antennas with an antenna spacing of $3\lambda \approx 36\,\text{cm}$. The measured amplitude differences between the transmit paths are about 0.30 dB, which is why we neglect these small amplitude imbalances at the transmitter. The phase imbalances at the transmitter are also neglected because we only focus on an antenna synthesis of the mobile receiver. The transmitter (the base station) is not synthesized in this work. The phase imbalances also do not affect the estimate of the channel capacity (eigenvalues) of the channel. So we get $\mathbf{D}_t = \mathbf{I}_M$ (the identity matrix of size M) for simplicity. Nevertheless transmitter amplitude

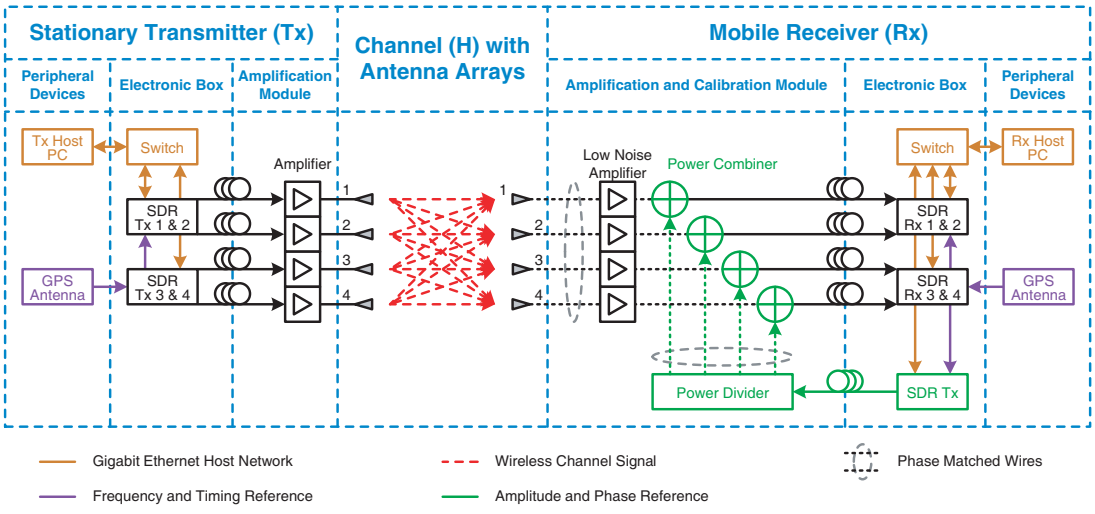

Figure 5. 4×4 MIMO channel measurement system hardware architecture overview.

Table 1. Measurement system parameters.

Parameter		Value
Number of Rx/Tx channels	$N \times M$	4×4
Center frequency	f_{RF}	2491.75 MHz
Sampling frequency	f_s	1 Msps
OFDM Subcarrier spacing	$\Delta f = \frac{f_s}{N_{\mathrm{FFT}}}$	1.953 kHz
FFT size	N_{FFT}	512 points
Used pilot carriers	N_{pilot}	16
Used reference carriers	N_{ref}	6
Pilot separation in frequency	$\Delta f_p = 5 \cdot \Delta f$	9.766 kHz
Pilot separation in time	$\Delta t_p = \frac{N_{\mathrm{FFT}}}{f_s}$	0.512 ms
Tx-Power @ antenna	P_{Tx}	24.5 dBm
Noise power	$P_N = k \cdot T \cdot f_s$	-113.9 dBm
Receiver noise figure	NF_{Rx}	4.0 dB
Tx-Antenna gain	G_{Tx}	4.7 dBi
Tx-Array element spacing	d_{Tx}	$3\,\lambda$
Rx-Antenna gain	$G_{\mathrm{Rx}} = G_{\mathrm{elem}}$	1.9 dBi
Rx-Array element spacing	d_{Rx}	$0.5\,\lambda$

(a) (b)

Figure 6. (a) Stationary transmitter setup and (b) mobile receiver setup.

and phase predistortion can easily be done as described in Section 3 in case, for example transmitter beamforming shall be investigated.

The mobile receiver buildup was integrated into a vehicle (see Fig. 6(b)). The rectangular receive antenna array consists of $N = 4$ omnidirectional monopole antennas with an antenna spacing of $\frac{\lambda}{2} \approx 6$ cm. The receiver electronic induced path imbalances (modeled with $\mathbf{D}_r = \mathbf{A}_r \cdot \mathbf{\Phi}_r$ in Section 3) are equalized with the help of the reference signal. The reference signal is distributed onto each receiver path with equal amplitude and equal phase. The reference signal is dynamically adapted in power to the received signal due to the near far effect in mobile communication to optimize the dynamic range of the receiver. The phase and amplitude matching of the reference distribution network and of the connections between the receive antennas and the calibration module (that also include the external receiver amplifiers) have been checked with the help of a network analyzer measurement. The measured differences that remain at the receiver are less than 3.23° in phase and less than 0.04 dB in amplitude.

Basic functionality tests of an OFDM communication as well as of a simple direction of arrival estimation/beamforming with the measurement system were completed successfully in our laboratory. That proofed the effectivity and the qualification of the channel measurement system for the subsequent application of the antenna synthesis on the measured channels.

5. MEASUREMENT RESULTS

The measured scenarios are located on the northern and southern campuses of the Karlsruhe Institute of Technology (KIT) in Karlsruhe, Germany (see Fig. 7).

The northern campus (see Fig. 7(a)) is an industrial park with mostly large buildings and open spaces between the buildings, which is used as the training scenario of the antenna synthesis. The transmitter was located on the roof of our partner institute's building in approximately 22.0 m height above ground. Measurements with an SNR lower than 10 dB were omitted. The whole measurement therefore comprises 3056 points (receiver locations) and the air-line distance between the stationary transmitter and the mobile receiver is between 50 m and 650 m.

The southern campus (see Fig. 7(b)) is an urban environment with large buildings and few high-rise buildings, which is used as the test scenario of the antenna synthesis. The transmitter was located on the roof of our institute's building in approximately 16.5 m height above ground. Measurements with an SNR lower than 10 dB were omitted. The whole measurement therefore comprises 2231 points (receiver locations) and the air-line distance between the stationary transmitter and the mobile receiver is between 50 m and 450 m.

Figure 7 also shows perimeters in steps of 100 m distance around the transmitter locations (white dashed circles). The received signals were recorded at the receiver locations with vertical copolarization while driving the streets of the campuses with a maximum speed of 10 $\frac{\text{km}}{\text{h}}$. The SNR of the 4×4 MIMO system in Fig. 7 was calculated on basis of the received pilot carrier power divided by the received power of the unused carriers. All measured points originate from non line-of-sight situations because the transmitter was always obstructed by the roof-edge or by other buildings or trees.

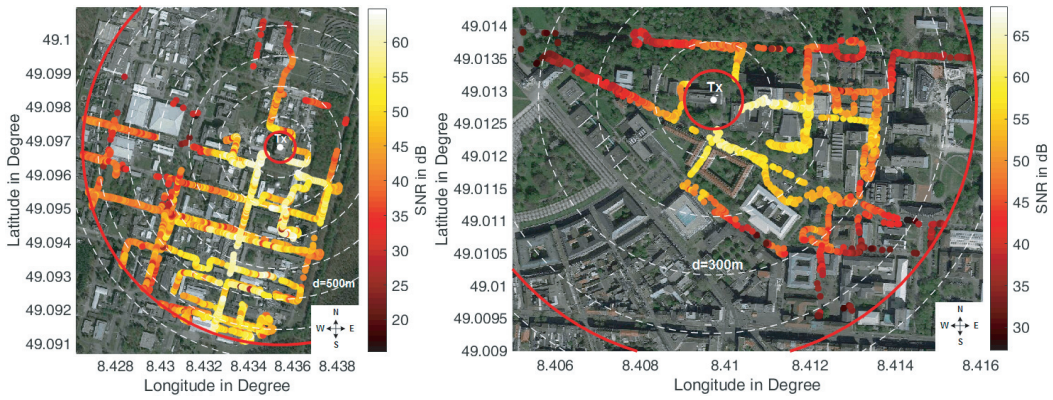

Figure 7. SNR at the receiver positions and maps of (a) the training scenario and (b) the test scenario of the antenna synthesis Google, Imagery ©2016, Cnes/Spot Image, DigitalGlobe, GeoBasis-DE/BKG, GeoContent.

The maximum speed of 10 $\frac{\text{km}}{\text{h}}$ yields a maximum doppler bandwidth of $B_D = 46.1\,\text{Hz}$ and a minimum coherence time of $T_{\text{coh}} = 21.7\,\text{ms}$. The pilot separation in time ($\Delta t_p = 0.512\,\text{ms}$) is well below the minimum coherence time of the channel and thus ensures a coherent channel within the measurement duration.

An assumed, maximum distance of the longest multipath of 3 km yields a maximum path delay of $\tau_{\max} = 10\,\mu\text{s}$ and a minimum coherence bandwidth of $B_{\text{coh}} = 100\,\text{kHz}$. The pilot separation in frequency ($\Delta f_p = 9.766\,\text{kHz}$) is well below the minimum coherence bandwidh of the channel and thus ensures a coherent channel within the measurement bandwidth.

6. ANTENNA SYNTHESIS PROCEDURE

The antenna synthesis procedure is published in [8]. The results rely on raytracing channel simulations and can be found in [9] and [10]. The idea behind the antenna synthesis is to optimize antenna

systems by using channel knowledge already in the design process of the antenna system. As a result fixed directional antenna radiation patterns are determined that optimize the mutual information for any given set of constraints such as the number of antennas, their geometrical size, polarization, the mounting positions and the frequency. The benefit is the reduction of hardware cost by employing a system with fewer but optimized antennas that outperform heuristically designed antenna systems.

First, the available antenna volume at the desired antenna mounting position is sampled with the help of several so-called sample antennas to determine the channel matrix **H**. The sample antennas are only needed during the synthesis process and gather the volume limited information about the communication channel.

In contrast to the work which was already published, we present an antenna synthesis that is based on dynamically measured MIMO channels in this work. Furthermore, we enhanced the synthesis method by applying the SVD for the similarity grouping and averaging step.

The whole antenna synthesis processing starting from the measured MIMO radio channel is depicted in Fig. 8 in terms of a block diagram.

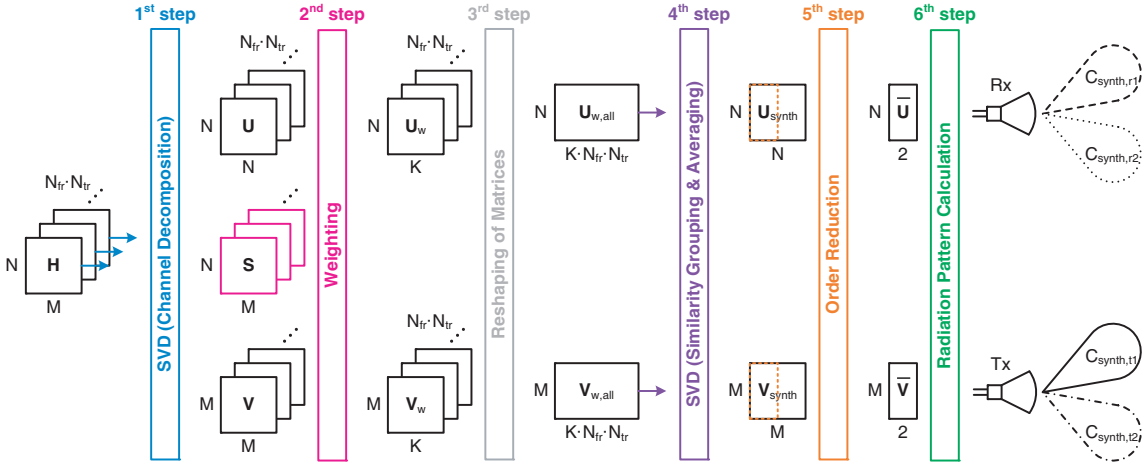

Figure 8. Antenna synthesis processing of two transmit and two receive antenna ports (radiation patterns) with dual application of SVD.

In the first step of the antenna synthesis procedure, the channel matrix is recorded by the use of transmitter and receiver sample antennas and calibrated according to Section 3. Afterwards, the channel matrix is decomposed into its unitary transmit and receive beamforming matrices (**V** and **U**) by applying the singular value decomposition (SVD) for each measurement in time dimension (for each snapshot or symbol) and for each subcarrier in frequency dimension:

$$\mathbf{H} = \mathbf{U} \cdot \mathbf{S} \cdot \mathbf{V}^{\dagger} \tag{13}$$

The beamforming vectors are the column vectors of the beamforming matrices, and the singular values $\sqrt{\lambda_k}$ are listed on the main diagonal of the matrix **S**:

$$\mathbf{U} = \{\vec{u}_1, \vec{u}_2, \ldots, \vec{u}_N\} \in \mathbb{C}^{N \times N} \tag{14}$$

$$\mathbf{V} = \{\vec{v}_1, \vec{v}_2, \ldots, \vec{v}_M\} \in \mathbb{C}^{M \times M} \tag{15}$$

$$\mathbf{S} = \operatorname{diag}\left(\sqrt{\lambda_1}, \sqrt{\lambda_2}, \ldots, \sqrt{\lambda_K}\right) \in \mathbb{R}^{N \times M} \text{ with } K = \operatorname{rank}(\mathbf{H}) \tag{16}$$

After the MIMO channel decomposition, we apply a weighting in the second step, which is optional. It can be formulated as a scaling of the beamforming vectors at the receiver:

$$\vec{u}_w(k, n_{fr}, n_{tr}) = \vec{u}(k, n_{fr}, n_{tr}) \cdot \sqrt{\lambda_k(n_{fr}, n_{tr})} \tag{17}$$

$$\mathbf{U}_w = \mathbf{U} \cdot \mathbf{S} = \{\vec{u}_{w1}, \vec{u}_{w2}, \ldots, \vec{u}_{wK}\} \in \mathbb{C}^{N \times K} \tag{18}$$

and at the transmitter:

$$\vec{v}_w(k, n_{fr}, n_{tr}) = \vec{v}(k, n_{fr}, n_{tr}) \cdot \sqrt{\lambda_k(n_{fr}, n_{tr})} \tag{19}$$

$$\mathbf{V}_w = \mathbf{V} \cdot \mathbf{S}^{\mathrm{T}} = \{\vec{v}_{w1}, \vec{v}_{w2}, \ldots, \vec{v}_{wK}\} \in \mathbb{C}^{M \times K} \tag{20}$$

The weighting uses the singular values $\sqrt{\lambda_k}$ as weighting factors to intensify and to control the averaging effect which can be found in the fourth step. It emphasizes the complex beamforming vectors which belong to large eigenvalues and extenuates the ones which belong to lower eigenvalues. k denotes the index of spatial subchannels with its maximum value $K = \mathrm{rank}(\mathbf{H})$, n_{tr} the index of time realizations and n_{fr} the index of frequency realizations according to Section 2.3.

Afterwards, a reshaping of matrices is implemented in the third step. It sorts the weighted complex beamforming vectors of all time realizations and of all frequency realizations into one large matrix $\mathbf{U}_{w,all}$ for the receiver and into one large matrix $\mathbf{V}_{w,all}$ for the transmitter:

$$\mathbf{U}_{w,all} = \{\vec{u}_w(1,1,1), \ldots, \vec{u}_w(K, N_{fr}, N_{tr})\} \in \mathbb{C}^{N \times K \cdot N_{fr} \cdot N_{tr}} \tag{21}$$

$$\mathbf{V}_{w,all} = \{\vec{v}_w(1,1,1), \ldots, \vec{v}_w(K, N_{fr}, N_{tr})\} \in \mathbb{C}^{M \times K \cdot N_{fr} \cdot N_{tr}} \tag{22}$$

The reshaping can be seen as a preparation for the similarity grouping and averaging that follows afterwards in step four. The similarity grouping and averaging of the complex beamforming vectors $\vec{v}_w$ and $\vec{u}_w$ over time (over several locations of a mobile system) matches the antenna systems at the transmitter and at the receiver to the communication channel by emphasizing the important predominant spatial directions with higher gain and suppressing other directions. For the first time, the similarity grouping and averaging step is performed by applying the SVD over time, frequency and space dimensions here as this is a novelty compared to the work in [8]:

$$\mathbf{U}_{w,all} \cdot \mathbf{U}_{w,all}^{\dagger} = \mathbf{U}_{\mathrm{synth}} \cdot \mathbf{S}_{r,\mathrm{synth}}^2 \cdot \mathbf{U}_{\mathrm{synth}}^{\dagger} \tag{23}$$

$$\mathbf{V}_{w,all} \cdot \mathbf{V}_{w,all}^{\dagger} = \mathbf{V}_{\mathrm{synth}} \cdot \mathbf{S}_{t,\mathrm{synth}}^2 \cdot \mathbf{V}_{\mathrm{synth}}^{\dagger} \tag{24}$$

The exactly same matrices $\mathbf{U}_{\mathrm{synth}}$ and $\mathbf{V}_{\mathrm{synth}}$ would result from just decomposing the matrices $\mathbf{U}_{w,all}$ and $\mathbf{V}_{w,all}$ with the help of the singular value decomposition (SVD) instead of decomposing the product with their complex conjugate transposed matrix ($\mathbf{U}_{w,all} \cdot \mathbf{U}_{w,all}^{\dagger}$ and $\mathbf{V}_{w,all} \cdot \mathbf{V}_{w,all}^{\dagger}$). But the computation time of the SVD is much faster in this way because we substitute the very large second dimension of $\mathbf{U}_{w,all}$ and $\mathbf{V}_{w,all}$, which is $K \cdot N_{fr} \cdot N_{tr}$ for the much smaller second dimension of the product $\mathbf{U}_{w,all} \cdot \mathbf{U}_{w,all}^{\dagger}$ and $\mathbf{V}_{w,all} \cdot \mathbf{V}_{w,all}^{\dagger}$, which is N or M.

The fifth step includes an order reduction by just employing the first two columns of $\mathbf{U}_{\mathrm{synth}}$ and $\mathbf{V}_{\mathrm{synth}}$ to get $\overline{\mathbf{U}}$ and $\overline{\mathbf{V}}$:

$$\overline{\mathbf{U}} = \{\vec{\overline{u}}_1, \vec{\overline{u}}_2\} \in \mathbb{C}^{N \times 2} \tag{25}$$

$$\overline{\mathbf{V}} = \{\vec{\overline{v}}_1, \vec{\overline{v}}_2\} \in \mathbb{C}^{M \times 2} \tag{26}$$

These two resulting columns represent the strongest predominant and important spatial directions of the determined MIMO channels, and the remaining columns are neglected.

The sixth step includes the determination of the synthesized antenna radiation patterns $C_{\mathrm{synth}}(\theta, \psi)$ on basis of the matrices $\overline{\mathbf{U}}$ and $\overline{\mathbf{V}}$. The Equations (27) and (28) in Section 7 give the calculation details.

In this work, we synthesized an automotive antenna that is mounted on the rooftop of a vehicle. So the sampling antennas were mounted on the rooftop (see Fig. 6(b)) and were configured to be the receiver during the channel measurements. The dimensions of the available antenna volume at this mounting location are about 6 cm × 6 cm × 10 cm. This volume was sampled using $N = 4$ sample antennas (monopoles) arranged in a square with $\frac{\lambda}{2} \approx 6\,\mathrm{cm}$ lateral length.

We distinguish between the training phase and the test phase of the synthesized antennas as the antenna synthesis procedure can be considered to be a kind of supervised learning. The grouping and averaging of the complex vectors $\vec{v}_k$ and $\vec{u}_k$ belongs to the training phase. This antenna radiation pattern optimization is based on the signals measured along the tracks of the training scenario. The comparison and evaluation of the performance of the antenna systems is done afterwards based on the

signals measured along the tracks of another scenario. This is called the test scenario, because it belongs to the test phase of the synthesized antennas. If the same dataset were used for both, the training and test phase, the results would be favourable because the optimization would be well suited for this data set.

7. ANTENNA SYNTHESIS RESULTS

In Section 7.1, we evaluate the shape of the resulting synthesized antenna radiation patterns. In addition, we evaluate their performance in terms of the channel capacities of a mobile single and a mobile double receiver path case in Section 7.2. And finally, we discuss the results and show the validation of the antenna synthesis approach in Section 7.3.

7.1. Evaluation of the Synthesized Antenna Radiation Patterns

The synthesized antenna radiation patterns $C_{\text{synth}}(\theta, \psi)$ depend on the radiation pattern of the sample antenna elements $C_{\text{elem}}(\theta, \psi)$ and on the group radiation patterns $C_{\text{gr}}(\theta, \psi)$:

$$C_{\text{synth}}(\theta, \psi) = C_{\text{elem}}(\theta, \psi) \cdot C_{\text{gr}}(\theta, \psi) \tag{27}$$

The group radiation patterns $C_{\text{gr}}(\theta, \psi)$ contain the antenna synthesis information. They result from the synthesized beamforming vectors $\vec{\overline{u}}_k$ through the array beamforming formula with x_p, y_p and z_p being the cartesian coordinates of the sample antenna elements ($z_p = 0$ was chosen):

$$C_{\text{gr}}(\theta, \psi) = \sum_{p=1}^{N} \overline{u}_p \cdot e^{j \cdot k \cdot [x_p \cdot \sin(\theta) \cdot \cos(\psi) + y_p \cdot \sin(\theta) \cdot \sin(\psi) + z_p \cdot \cos(\theta)]} \tag{28}$$

Fig. 9 depicts the measured sample antenna element radiation pattern $C_{\text{elem}}(\theta)$ as it was used during the channel sampling. The radiation pattern measurement was performed in our institute's anechoic antenna measurement chamber. The gain is $G_{\text{elem}} = 1.9\,\text{dBi}$. Ideally the sample antenna element radiation pattern should approximate an isotropic radiator. This can easily be done in channel simulations. But considering the channel measurements, we have to arrange a compromise as an isotropic radiator is not realizable. This brings the disadvantage of several nulls or low-gain directions into the sample antenna element radiation pattern. These nulls induce blind spots during the antenna synthesis procedure. The first null can be found in zenith direction ($\theta_{n1} = 0°$) and is not considered problematic since we do not expect power impinging from zenith onto the sample antenna array in the urban base station-to-mobile scenario. The second null is at $\theta_{n2} = 52°$ or $308°$. This null direction decreases the potential performance of the antenna synthesis because it is not possible to detect or to emphasize possible multipaths that may impinge onto the sample antenna array from these directions. The antenna synthesis procedure is blind in these null directions. In addition, the sample antenna element radiation pattern experiences distortions as a result of mutual coupling with the neighboring sample antennas. That additionally degrades the performance of the antenna synthesis.

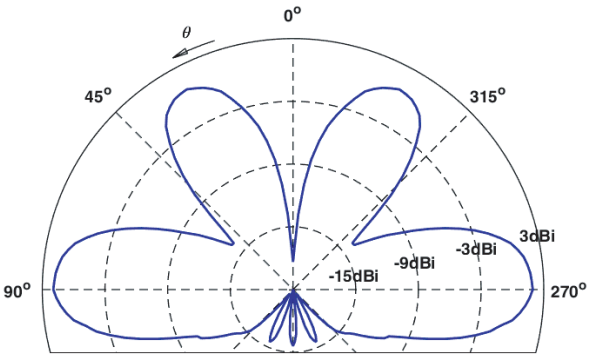

Figure 9. Sample antenna element radiation pattern $|C_{\text{elem}}(\theta)|$ measured in the vertical plane.

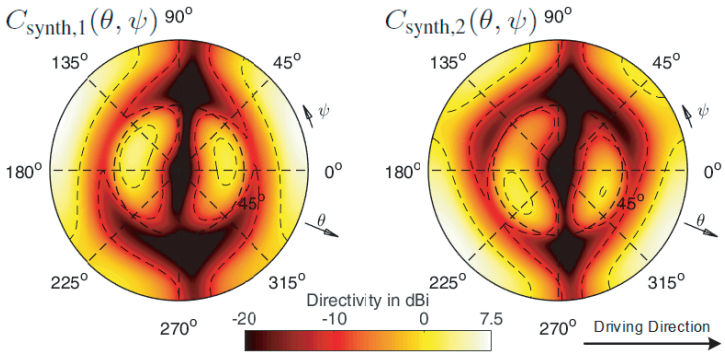

Figure 10. Synthesized antenna radiation patterns $C_{\text{synth},1}(\theta,\psi)$ and $C_{\text{synth},2}(\theta,\psi)$ for $\theta = 0° \ldots 90°$ and $\psi = 0° \ldots 360°$ (upper hemisphere only).

Figure 10 displays the first two synthesized antenna radiation patterns $C_{\text{synth},1}(\theta,\psi)$ and $C_{\text{synth},2}(\theta,\psi)$ for the upper hemisphere. The elevation angle θ is displayed as the radial component from 0° (zenith direction) to 90°, and the azimuth angle ψ is displayed as the tangential component of the plot ranging from 0° to 360°. The driving direction of the mobile receiver is specified in Fig. 10 and is directed at $\theta = 90°$ and $\psi = 0°$. The directivities are $D_{\text{synth},1} = 7.2\,\text{dBi}$ and $D_{\text{synth},2} = 7.1\,\text{dBi}$ respectively. An efficiency factor of $\mu = 1$ was assumed. Hence the directivities are shown. We can identify two main beam directions of the first synthesized antenna radiation pattern $C_{\text{synth},1}(\theta,\psi)$. They can be found at $(\theta_{\text{max1}}, \psi_{\text{max1}}) = (90°, 158°)$ and $(90°, 18°)$. The second synthesized antenna radiation pattern $C_{\text{synth},2}(\theta,\psi)$ exhibits its main beam directions at $(\theta_{\text{max2}}, \psi_{\text{max2}}) = (90°, 214°)$ and $(90°, 330°)$. In summary, we can identify a strong weighting of $C_{\text{synth},1}$ in and against the driving direction with a tilt of about 20° to the left and a strong weighting of $C_{\text{synth},2}$ to both of the diagonal directions to the right.

7.2. Evaluation and Comparison of the Channel Capacities

We assumed a transmit power of $P_{\text{Tx}} = 40\,\text{dBm}$ and a noise power of $\sigma^2 = -92\,\text{dBm}$ (with a bandwidth of $B = 20\,\text{MHz}$ and a noise figure of $NF = 9\,\text{dB}$) for the calculation of the channel capacity. These values correspond to a common LTE communication with the base station as the transmitter. Furthermore, we assumed that only the receiver had channel knowledge (channel state information, CSI). Thus the channel capacity was determined according to [1, 13].

The capacity of the channel with the omnidirectional antennas was calculated without any antenna synthesis since the sample antenna elements already provided an omnidirectional radiation pattern. Therefore, the 2×4 channel including the omnidirectional receiver antennas $\mathbf{H}_{\text{omni}}(t)$ can be obtained from the measured 4×4 channel $\mathbf{H}(t)$ through an order reduction step according to the one in Fig. 8 and as described in [5].

$$C_{\substack{\text{omni} \\ \text{CSI @ Rx}}}(t) = \log_2 \left[\det \left(\mathbf{I}_N + \frac{P_{\text{Tx}}}{M \cdot \sigma^2} \cdot \mathbf{H}_{\text{omni}}(t) \cdot \mathbf{H}_{\text{omni}}(t)^\dagger \right) \right] \tag{29}$$

The capacity of the 2×4 channel with the adaptive beamforming was calculated with the beamforming matrices $\mathbf{U}(t)$ (see Fig. 8). These beamforming matrices $\mathbf{U}(t)$ are time dependent because they realize an adaptive beamforming that is optimal for every measured receiver location within the scenario. The channel including the adaptive beamforming can be obtained from the measured 4×4 channel through the matrix multiplication $\mathbf{H}_{\text{adapt}}(t) = \mathbf{U}(t)^\dagger \cdot \mathbf{H}(t)$. And its channel capacity is determined as

$$C_{\substack{\text{adapt} \\ \text{CSI @ Rx}}}(t) = \log_2 \left[\det \left(\mathbf{I}_N + \frac{P_{\text{Tx}}}{M \cdot \sigma^2} \cdot \mathbf{U}(t)^\dagger \cdot \mathbf{H}(t) \cdot \mathbf{H}(t)^\dagger \cdot \mathbf{U}(t) \right) \right] \tag{30}$$

The capacity of the 2×4 channel with the synthesized antennas was calculated with the constant beamforming vectors included in $\overline{\mathbf{U}}$, which do not depend on time (see Fig. 8). Therefore, the channel

including the synthesized receiver antennas can be obtained from the measured 4×4 channel through the matrix multiplication $\mathbf{H}_{\text{synth}}(t) = \overline{\mathbf{U}}^{\dagger} \cdot \mathbf{H}(t)$. And its channel capacity is determined as

$$C_{\substack{\text{synth} \\ \text{CSI @ Rx}}}(t) = \log_2 \left[\det \left(\mathbf{I}_N + \frac{P_{\text{Tx}}}{M \cdot \sigma^2} \cdot \overline{\mathbf{U}}^{\dagger} \cdot \mathbf{H}(t) \cdot \mathbf{H}(t)^{\dagger} \cdot \overline{\mathbf{U}} \right) \right] \tag{31}$$

The channel capacity $C_{\substack{\text{omni} \\ \text{CSI @ Rx}}}$ of the system with omnidirectional antenna radiation patterns can be considered to be the benchmark for comparison to the channel capacity $C_{\substack{\text{synth} \\ \text{CSI @ Rx}}}$ of the synthesized system. The difference between these two channel capacities is a measure for the benefit that comes with the antenna synthesis.

The channel capacity $C_{\substack{\text{adapt} \\ \text{CSI @ Rx}}}$ of the adaptive system can be considered to be the maximum upper bound of the channel capacity $C_{\substack{\text{synth} \\ \text{CSI @ Rx}}}$ of the synthesized system. This maximum upper bound can not be reached by the non-adaptive synthesized antenna system because it can not adapt to the channel during the test phase because it employs fixed antenna radiation patterns in contrast to the system with adaptive beamforming.

Figure 11 gives the cumulative distribution functions (CDF) of the channel capacities for the omnidirectional (omni), the synthesized (synth) and for the adaptive (adapt) antenna radiation patterns at the receiver for $M = 4$ transmitters. The black vertical lines at the locations of the data markers indicate the 95% confidence intervals (for $\alpha = 0.05$).

The MISO case includes a single receiver path. In the synthesized MISO case $C_{\text{synth},1}(\theta, \psi)$ was applied. And in the adaptive MISO case an adaptive optimal beamforming with the four omnidirectional sampling antennas but only one single receiver path was applied. The MIMO case includes two receiver paths. In the synthesized case $C_{\text{synth},1}(\theta, \psi)$ and $C_{\text{synth},2}(\theta, \psi)$ were applied. And in the adaptive MIMO case an adaptive optimal beamforming with the four omnidirectional sampling antennas but two receiver paths was applied.

The difference in the $p_{\text{out}} = 10\%$ outage capacity C_{out} between the omnidirectional and the synthesized case is 0.69 $\frac{\text{Bit}}{\text{s·Hz}}$ for the MISO (single receiver path) case and 0.98 $\frac{\text{Bit}}{\text{s·Hz}}$ for the MIMO (double receiver path) case. The differences indicate a small but significant channel capacity increase by means of the antenna synthesis because the confidence intervals do not touch or overlap each other.

The difference in the $p_{\text{out}} = 10\%$ outage capacity C_{out} between the omnidirectional and the adaptive case is 1.74 $\frac{\text{Bit}}{\text{s·Hz}}$ for the MISO (single receiver path) case and 2.17 $\frac{\text{Bit}}{\text{s·Hz}}$ for the MIMO (double receiver path) case. The differences indicate the channel capacity increase by means of the adaptive beamforming as it was expected.

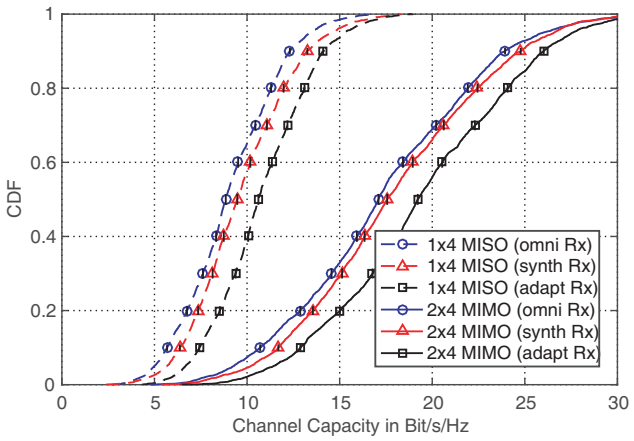

Figure 11. Channel capacity of MISO and MIMO systems with $M = 4$ transmitters, omnidirectional respectively synthesized antenna radiation patterns at the mobile receiver, $P_{\text{Tx}} = 40\,\text{dBm}$.

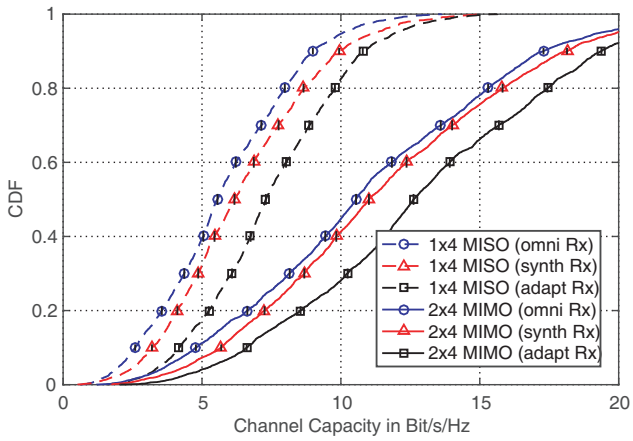

Figure 12. Channel capacity of MISO and MIMO systems with $M = 4$ transmitters, omnidirectional respectively synthesized antenna radiation patterns at the mobile receiver, $P_{\text{Tx}} = 30\,\text{dBm}$.

Figure 12 displays cumulative distribution functions (CDF) of the mentioned systems but here for a lower transmit power of $P_{\mathrm{Tx}} = 30\,\mathrm{dBm}$. Please note the different scaling of the abscissa when comparing it to Fig. 11.

The difference in the $p_{\mathrm{out}} = 10\%$ outage capacity C_{out} between the omnidirectional and the synthesized case is $0.60\,\frac{\mathrm{Bit}}{\mathrm{s{\cdot}Hz}}$ for the MISO (single receiver path) case and $0.91\,\frac{\mathrm{Bit}}{\mathrm{s{\cdot}Hz}}$ for the MIMO (double receiver path) case. This confirms that the performance of the synthesized antenna systems stays superior even with a 10 dB lower transmit power or SNR respectively.

The difference in the $p_{\mathrm{out}} = 10\%$ outage capacity C_{out} between the omnidirectional and the adaptive case is $1.58\,\frac{\mathrm{Bit}}{\mathrm{s{\cdot}Hz}}$ for the MISO (single receiver path) case and $1.83\,\frac{\mathrm{Bit}}{\mathrm{s{\cdot}Hz}}$ for the MIMO (double receiver path) case.

7.3. Discussion and Validation of the Antenna Synthesis Results

Mobile urban radio channels in principle have a random character that corresponds to the Rayleigh distribution if we assume non line-of-sight situations [13]. But there are also principal predominant directions or signal parts respectively that appear more often than other signal parts and significantly influence the SNR. This can be observed from the channel capacity evaluations in Section 7.2. These systematic signal parts are superposed to the purely random Rayleigh character. The antenna synthesis is a method to identify these systematic signal parts and to benefit from them. These principal predominant directions and channel characteristics found by the antenna synthesis method depend on the scenarios that contribute to the averaging step during the antenna synthesis procedure. To avoid adaption effects during the evaluation of the antenna synthesis results we distinguish strictly between the training phase and the test phase as explained in the endmost part of Section 6. Due to this the results shown above in Section 7 already contain two different but similar scenarios or measurement runs respectively. Thus the antenna synthesis is beneficial for the two scenarios mentioned.

In addition to the channel measurements described in this work, the antenna synthesis results were also validated by the use of deterministic radio channel simulations based on ray-optical methods [9, 10]. These simulations employ a theoretical description and analysis of the wave propagation effects by the use of a raytracing algorithm. The system simulator used therein was in turn verified and validated in terms of reference measurements of the simulated wave propagation scenarios and proofed very good agreement between measurements and simulations [15, 16].

In [9], car-to-car communication was investigated, and the antenna synthesis was applied to different antenna mounting positions around a vehicle. The antenna positions with a visibility region in and against the driving direction performed best. The authors also found that the main interaction plane of the simulated wave propagation is the azimuth plane around $\theta \approx 90°$. The antenna radiation patterns should focus in these directions with maximum antenna gain to achieve a maximized SNR and a maximized channel capacity. The reason for that effect is given in the surrounding buildings that act like a waveguide along the street canyons. These results agree with the synthesized antenna radiation patterns found in our work (see Fig. 10) and therefore confirm our findings that are based on channel measurements of different but similar urban communication scenarios.

In [10], car-to-car communication was also investigated, and the antenna synthesis was additionally performed for a double receiver path case. The first synthesized receiver radiation pattern for the automotive roof antenna location focuses in and against the driving direction. The second synthesized radiation pattern is tilted towards the left and right diagonals ($\theta = 90°, \psi \approx \pm 45°$). These results also agree very well with the synthesized antenna radiation patterns found in our work (see Fig. 10). This also reassures our results based on measured urban communication scenarios that are different but similar to the ones in [10].

Due to these corresponding findings in different but similar scenarios, we can claim a considerable validity of our main antenna synthesis results for mobile urban radio channels. But still the optimal synthesized antenna radiation patterns and their performance depend, to a certain extent, on the specific urban areas under investigation and can not be considered absolutely universal for every imaginable urban scenario.

8. CONCLUSION

For the first time, an antenna synthesis is done on the basis of a dynamically measured radio channel sampling of a whole real world scenario (see Section 5). An antenna synthesis based on measured channels faces additional technical problems compared to an antenna synthesis that is based on simulated channels. On the one hand, there is mutual coupling between neighboring sample antenna elements, and on the other hand, there are blind spots that can not be involved in the antenna synthesis. Both effects downgrade the potential performance of the antenna synthesis.

Nevertheless, the synthesized radiation patterns that result from the channel measurements (see Section 7) confirm the synthesized radiation patterns that follow from the raytracing channel simulations in [8–10].

The focus of the first synthesized antenna radiation pattern in and against the driving direction with a tilt to the left can be explained by the waveguide effect in urban street canyons, that has also been experienced in [3]. The focuses of both synthesized antenna radiation patterns (in and against the driving direction with a tilt to the left/to both of the diagonal directions to the right) correlate very well with the results in [9] and [10]. Reichardt et al. applied the antenna synthesis on raytracing channel simulations and discovered that the main interaction plane was the azimuth one (for $\theta \approx 90°$) especially in non line-of-sight situations of a car-to-car communication. The measurements conducted in our work exclusively involve non line-of-sight scenarios between a base station and a vehicle.

The benefit of the antenna synthesis is shown in this paper. It emerges without any additional system cost compared to conventional antenna systems. The synthesized single and multiple antenna systems achieve better performances in terms of channel capacity than conventional omnidirectional antennas as they are used in commercial automotive rooftop antennas (see Section 7). Even though the training scenario (industrial park) and test scenario (urban environment) do not exhibit exactly same characteristics, the benefit of the antenna synthesis is considerable.

If we consider that receivers with omnidirectional antennas exploit none (0%) of the total optimization potential of the $p_{\text{out}} = 10\%$ outage capacity C_{out} that result from antenna radiation pattern matching to the channel, then we can say that a receiver with adaptive optimal beamforming exploits 100%. The proposed synthesized antenna systems achieve 39.7% for the MISO case and 45.2% for the MIMO case at 40 dBm transmit power. For 30 dBm transmit power, the synthesized antenna systems achieve 38.0% for the MISO case and 49.7% for the MIMO case. It implies that by using non-adaptive (fixed) synthesized antenna radiation patterns, we achieve high optimization potentials without the need for any channel estimation during operation compared to an expensive adaptive beamforming receiver system that has to estimate the channel continuously to be able to react to its changes.

The comparison of omnidirectional, synthesized and adaptive antenna systems was demonstrated for two different transmit power or SNR cases, respectively. From it we can conclude that synthesized antennas have an improved matching relating to the considered radio channel compared to omnidirectional ones.

ACKNOWLEDGMENT

This work was supported by the German Research Foundation (DFG) in the context of the project OASE. The authors would also like to thank Ronald Vester, Mirko Nonnenmacher and Andreas Gallego Klose for their help in manufacturing the antennas and in building up the measurement system. We also thank Prof. John Jelonnek and Sebastian Ruess from our partner institute IHM for their support during the measurement campaign at the northern campus of Karlsruhe Institute of Technology (KIT).

REFERENCES

1. Foschini, G. J. and M. J. Gans, "On limits of wireless communications in a fading environment when using multiple antennas," *Wirel. Pers. Commun.*, Vol. 6, No. 3, 311–335, Mar. 1998.
2. Trautwein, U., C. Schneider, and R. Thoma, "Measurement-based performance evaluation of advanced MIMO transceiver designs," *EURASIP Journal on Advances in Signal Processing*, Vol. 2005, No. 11, 298213, 2005.

3. Kim, M.-D., J. Lee, J. Liang, and J. Kim, "Multipath characteristics for mobile to mobile direct communications based on channel measurement in urban street grid environments," *2014 16th International Conference on Advanced Communication Technology (ICACT)*, 146–150, Feb. 2014.
4. Abbas, T., J. Nuckelt, T. Kurner, T. Zemen, C. Mecklenbrauker, and F. Tufvesson, "Simulation and measurement-based vehicle-to-vehicle channel characterization: Accuracy and constraint analysis," *IEEE Transactions on Antennas and Propagation*, Vol. 63, No. 7, 3208–3218, Jul. 2015.
5. Caban, S., J. Garcia Naya, and M. Rupp, "Measuring the physical layer performance of wireless communication systems: Part 33 in a series of tutorials on instrumentation and measurement," *IEEE Instrumentation Measurement Magazine*, Vol. 14, No. 5, 8–17, Oct. 2011.
6. Taparugssanagorn, A., M. Alatossava, V. M. Holappa, and J. Ylitalo, "Impact of channel sounder phase noise on directional channel estimation by space-alternating generalised expectation maximisation," *IET Microwaves, Antennas and Propagation*, Vol. 1, No. 3, 803–808, Jun. 2007.
7. Taparugssanagorn, A. and J. Ylitalo, "Characteristics of short-term phase noise of MIMO channel sounding and its effect on capacity estimation," *IEEE Transactions on Instrumentation and Measurement*, Vol. 58, No. 1, 196–201, Jan. 2009.
8. Mahler, T., L. Reichardt, C. Heine, M. Pauli, and T. Zwick, "Channel based design of systems with multiple antennas," *Progress In Electromagnetics Research B*, Vol. 64, 63–81, 2015.
9. Reichardt, L., T. Mahler, T. Schipper, and T. Zwick, "Influence of single and multiple antenna placements on the capacity of c2c communication systems," *2013 European Microwave Conference (EuMC)*, 720–723, Oct. 2013.
10. Reichardt, L., T. Mahler, Y. L. Sit, and T. Zwick, "Using a synthesis methodology for the design of automotive antenna systems," *2013 7th European Conference on Antennas and Propagation (EuCAP)*, 1600–1604, Apr. 2013.
11. Takada, J., K. Sakaguchi, and K. Araki, "Development of high resolution mimo channel sounder for the advanced modeling of wireless channels," *2001 Asia-Pacific Microwave Conference, 2001. APMC 2001*, Vol. 2, 563–568, Dec. 2001.
12. Konishi, Y., M. Kim, M. Ghoraishi, J. Takada, S. Suyama, and H. Suzuki, "Channel sounding technique using mimo software radio architecture," *Proceedings of the 5th European Conference on Antennas and Propagation (EUCAP)*, 2546–2550, Apr. 2011.
13. Tsoulos, G. V. H., ed., *MIMO system technology for wireless communications*, Ser. Electrical engineering & applied signal processing series, CRC Press, Boca, Raton, Fla. [u.a.], 2006.
14. http://www.ettus.com/, "USRP X310 product page," 2016, [Online] Available: http://www.ettus.com/product/details/X310-KIT. [Accessed: 14-Jan-2016].
15. Fugen, T., J. Maurer, T. Kayser, and W. Wiesbeck, "Capability of 3-D ray tracing for defining parameter sets for the specification of future mobile communications systems," *IEEE Transactions on Antennas and Propagation*, Vol. 54, No. 11, 3125–3137, Nov. 2006.
16. Reichardt, L., J. Maurer, T. Fugen, and T. Zwick, "Virtual drive: A complete V2X communication and radar system simulator for optimization of multiple antenna systems," *Proceedings of the IEEE*, Vol. 99, No. 7, 1295–1310, Jul. 2011.